Chinese Chemical Letters 35 (2024) 109523

Contents lists available at ScienceDirect

Chinese Chemical Letters

journal homepage: www.elsevier.com/locate/cclet

Red-emissive carbon quantum dots minimize phototoxicity for rapid and long-term lipid droplet monitoring

Fengkai Zou[a,b,1], Borui Su[c,1], Han Leng[d], Nini Xin[c], Shichao Jiang[c], Dan Wei[c], Mei Yang[d], Youhua Wang[a,*], Hongsong Fan[c,*]

[a] Department of Orthopedics, Affiliated Hospital of Nantong University, Nantong 226001, China
[b] Graduate School, Dalian Medical University, Dalian 116044, China
[c] National Engineering Research Center for Biomaterials, College of Biomedical Engineering, Sichuan University, Chengdu 610064, China
[d] School of Chemistry and Chemical Engineering, Liaoning Normal University, Dalian 116029, China

ARTICLE INFO

Article history:
Received 9 November 2023
Revised 11 January 2024
Accepted 12 January 2024
Available online 20 January 2024

Keywords:
Carbon quantum dots
Solvatochromism
Lipid droplet probe
Fluorescence imaging
Wash-free

ABSTRACT

Long-term fluorescence monitoring of subcellular organelles is crucial for cellular physiology and pathology studies. Lipid droplets (LDs) are increasingly recognized for their involvement in various biological processes, to influence disease development through diverse behaviors However, existing LD probes face challenges in achieving high targeting and long-term monitoring due to poor photostability and long-term phototoxicity. Carbon quantum dots (CQDs) have gained prominence due to their exceptional fluorescence properties, but their prevalent blue excitation wavelength presents difficulties for long-term imaging. Herein, we synthesized red-emissive carbon quantum dot (R-CQDs) with superior photobleaching resistance and red-emission, thus enabling harmlessly fluorescence monitoring of cells longer than 3 h. In addition, R-CQD exhibits suitable amphiphilicity and remarkable solvatochromic effect, allowing rapid targeting to LDs for immediate imaging without cumbersome washing steps. Hence, R-CQD shows high performance for extended observation of dynamic LD behavior in various biological processes, which is confirmed by documenting the course of LDs during starvation as well as lipotoxicity. Compared to commercial probes, R-CQD extends live cell imaging time by at least 9-fold, facilitating the study of LD behavioral characteristics under diverse physiological or pathological conditions. This work provides a reliable fluorescence tool for tracking intercellular microenvironment dynamically thus to understand the divers biological or disease mechanism.

Fluorescence imaging has been widely employed for observing the intracellular microenvironment due to its good specificity and high sensitivity [1–4]. Utilizing diverse fluorescent probes, this technique distinguishes objects of interest from complex backgrounds, providing high spatial and temporal resolution [5–7]. However, most current fluorescence images of organelle morphology are derived from fixed or static specimens [8,9], which limits the revelation of dynamic processes. To track biological processes over the long term, it is crucial to ensure the prolonged viability of cells and the stability of fluorescent probes [10–12]. Numerous small-molecule dyes based on xanthene, cyanine, oxazine, and dipyrromethene boron difluoride (BODIPY) have been developed for super-resolution bioimaging, but the prevalent issue of self-quenching due to the small Stokes shift persists [13]. Additionally, poor stability, insufficient hydrophilicity, and undesired self-aggregation impede further bioimaging applications. Therefore, there is an urgent need to develop a fluorescent probe that can specifically target subcellular organelles with good stability and cytocompatibility in order to realize long-term dynamic tracking and to clarify progression of biological events.

Carbon quantum dots (CQDs), as an organic fluorescent nanomaterial exhibiting large Stokes shifts, high resistance to photobleaching, high fluorescence quantum yield, and low biotoxicity, have emerged as attractive candidates for bioimaging [14–20]. Similar to small-molecule dyes, CQDs with suitable functional groups will confer specific organelle targeting capabilities, such as mitochondria-targeted CQD with positive surface charge [21], lysosome-targeted CQD with morpholine-moieties [22–24], endoplasmic reticulum-targeted CQD with laurylamine-functionalization [23], and lipid droplet (LD)-targeted CQD with lipophilic and hydrophilic groups [25]. However, not all of them meet the requirement of long-wavelength fluorescence imaging

* Corresponding authors.
E-mail addresses: wangyouhua99@163.com (Y. Wang), hsfan@scu.edu.cn (H. Fan).
[1] These authors contributed equally to this work.

https://doi.org/10.1016/j.cclet.2024.109523
1001-8417/

Scheme 1. Synthetic route of R-CQDs for lipid droplets long-term monitoring.

due to the on high-energy blue or even violet laser irradiation, leading to the accumulation of reactive oxygen species (ROS) and causing substantial cellular damage, potentially influencing experimental outcomes [26–29]. Some previous studies have manifested that red-shifted lasers is highly effective in mitigating phototoxicity. Even a subtle red-shift from blue light can significantly enhance long-term cellular activity [26,30]. Therefore, developing CQDs with longer fluorescence wavelengths is crucial to achieving long-term tracking monitoring of organelles in biological processes.

Recently, the importance of LDs in various biological process has caused increasing interests. Generally, LD is regarded as a highly conserved organelles, besides the primarily tasking with lipid storage, transportation, and metabolic regulation. LDs are found collaborate with other organelles, such as mitochondria and lysosomes, to execute various cellular physiological activities [31–36]. More importantly, the behavior of LDs in cells undergoes subtle changes in patients afflicted with diseases like metabolic syndrome, cancer, and neurodegenerative disorders [37–42]. The behavior of LDs can either alleviate or exacerbate disease progression. Consequently, investigating the therapeutic use of LDs while minimizing side effects becomes a research area of significant interest. Detailed recording of LD behavior could yield crucial data elucidating the relationship between LD behavior and the disease process [43,44].

Hence, we aim to address the limitations of commercial probes, such as short excitation wavelengths and susceptibility to photobleaching, hindering long-term LDs monitoring. Our design focuses on key factors: first, recognizing the hydrophobic nature of LDs, we prioritize achieving appropriate amphiphilicity for effective LDs targeting. Second, we aim to enhance the conjugated core's size and introduce N doping to reduce the highest occupied molecular orbital-lowest unoccupied molecular orbital (HOMO-LUMO) band gap, enabling a significant red-shift in fluorescence. Finally, the functional groups contained in the raw materials for the synthesis of CQDs are likely to be retained in the products. Therefore, we prepare red-emissive carbon quantum dot (R-CQDs) by mixing amino-rich *p*-phenylenediamine (*p*-PD), methyl-rich *N*,*N*-dimethylformamide (DMF) and 1,10-phenanthroline (phen) aiming to achieve significant solvatochromic effects, appropriate amphiphilicity and red-shifting fluorescence, and thus to realize LD-targeting for convenient wash-free LDs imaging, as well as reduced phototoxicity to associate long-term LDs monitoring. Afterwards, the new R-CQD probe is used for dynamic monitoring of LDs in various pathologies, including starvation and lipotoxicity, fully demonstrating the potential of R-CQD for LDs long-term monitoring (Scheme 1). Thus, the present work expands the application of CQDs as fluorescent probes and provides a reliable tool for studies related to the dynamic behavior of LDs under physiological and pathological conditions.

The R-CQD was prepared with p-PD and phen as precursor through a one-step high-temperature (HT) solvothermal method in DMF (Fig. 1a). The resulting R-CQD was then systematically characterized. Transmission electron microscopy (TEM) images (Fig. 1b) revealed a spherical structure of the R-CQD with uniform size (~3 nm), and no apparent aggregation was observed. In addition, the high-resolution transmission electron microscopy (HRTEM) image of R-CQD showcased an ordered crystal structure (Fig. 1c), featuring a crystal plane spacing of 0.207 nm that is clearly visible (Fig. 1d). This spacing corresponds to the (100) crystallographic plane of graphite. In addition, there is a distinct 25° peak in the X-ray diffractometer (XRD) image (Fig. S1 in Supporting information) of the R-CQD, which corresponds to the 0.36 nm crystal spacing of the graphite (002) crystal plane [45]. These findings affirm the successful synthesis of CQDs through the solvothermal method.

The Fourier transform infrared spectroscopy (FTIR) reveals the presence of abundant amino and methyl functional groups on the surface of R-CQD. As shown in Fig. 1e, the absorption bands in the range of 3100–3500 cm^{-1} typically signify the stretching vibrations of O–H and N–H groups [45]. Simultaneously, the absorption peak at 1509 cm^{-1} corresponds to the bending vibration of N–H. The overlapping stretched absorption bands at 2920, 2850, and 2890 cm^{-1} signify the stretching vibration of C–H groups, while the absorption peak at 1428 cm^{-1} corresponds to the bending vibration of C–H. Furthermore, characteristic peaks at 841 and 733 cm^{-1} correspond to the C–H out-of-plane bending vibration of aromatic benzene with a phenazine backbone. Additionally, the absorption peak associated with the C=C/C=O bond manifests at 1660 cm^{-1}. The abundance of amino and methyl groups on the surface of R-CQD imparts it with suitable amphiphilicity.

^{1}H NMR spectra were employed to confirm the structure of R-CQD. As shown in Fig. 1f, signals in the range of 6.5–8 ppm should come from H in the aromatic structure, while the -NH_2 peak appeared near 2.5 ppm, indicates partial retention of the precursor moiety. Additionally, an O–H peak near 3.5 ppm was observed. Subsequently, X-ray photoelectron spectroscopy (XPS) analysis was further used to analyze the chemical composition of R-CQD. The complete XPS spectrum (Fig. 1g) indicates that R-CQD comprises elements C, O, and N in proportions of 74.38%, 13.29%, and 12.33%, respectively. The high-resolution spectra confirmed that the two combine peaks at 284.8 and 285.6 in the C 1s spectrum which represent the chemical structures of C–C/C=C and -N/C–O (Fig. 1h). The two fitted peaks at 399.1 and 400.2 eV in the N 1s spectrum represent pyridine N and pyrrole N (Fig. 1i). The two fitted peaks at 532.1 and 533.3 eV in the O 1s spectrum describe the presence of C=O and C–O [46], respectively (Fig. 1j). These results confirm the successful doping of the N element, which has the potential to reduce the HOMO-LUMO band gap of R-CQD, leading to a fluorescence red-shift. Meanwhile, the abundance of amino and alkane groups on the surface will endow the R-CQD with excellent amphiphilicity.

The optical properties of R-CQD were meticulously characterized. Initially dispersing in glyceryl trioleate (the main component of LDs) to simulate the low-polar environment of LDs (Fig. 2a), R-CQD exhibited mainly 590 nm emission excited by 510 nm light, corresponding to an 80 nm Stokes shift (as contrast, the Stokes shift of commercial BODIPY is 10 nm). The fluorescence lifetime (Fig. 2b) and quantum yield (QY) (Fig. 2c and Fig. S2 in Supporting information) of R-CQD in LDs like environment were also tested, and the results showed that R-CQD had two fluorescence centers with lifetimes of 2.444 ns and 0.115 ns, respectively, and exhibited a QY of about 29.18%, which is relatively high among the reported red-emissive CQDs [47–49]. This level of QY is considered high enough for effective fluorescence imaging of cells. Notably, when compared to many reported QYs of red-emissive CQDs, which of-

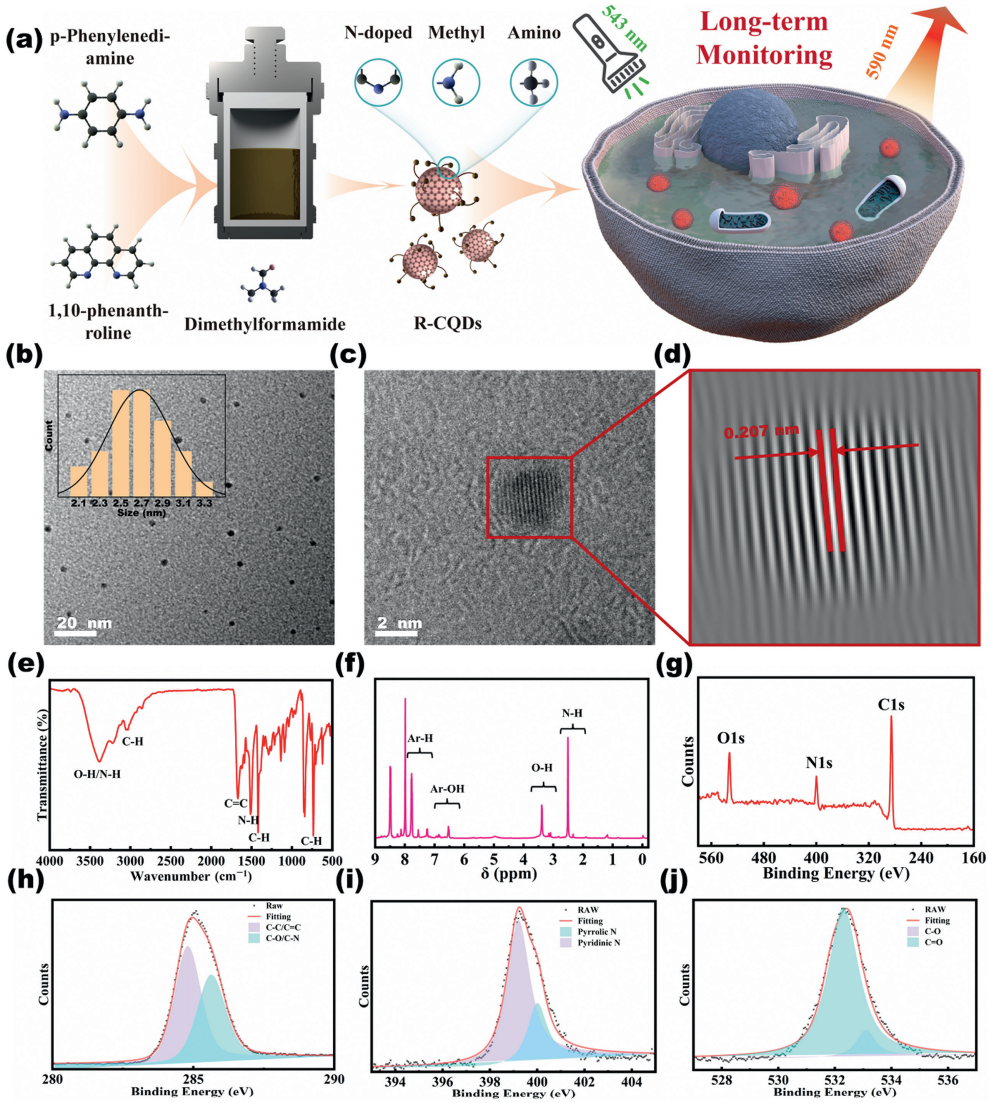

Fig. 1. Synthesis and characterization of CQDs. (a) Schematic of the R-CQD synthesis process. (b) TEM images of R-CQD, and particle size distribution. (c) HRTEM image of R-CQD. (d) Enlarged and fast Fourier transform (FFT) transformed HRTEM image highlighting the 0.207 nm crystal plane spacing. (e) FTIR of R-CQD. (f) ^{1}H NMR spectrum of R-CQD. (g) XRD spectra and high-resolution, (h) C 1s, (i) N 1s and (j) O 1s of R-CQD.

ten fall into single-digit percentages, the fluorescence performance of R-CQD stands out as superior.

To explore the solvatochromic effect of R-CQD, we dispersed R-CQD in 1,4-dioxane with gradually doped water and scanned the changes in excitation-emission matrices (EEM) during the process. The results showed a red-shift of nearly 30 and 50 nm in fluorescence excitation and emission, respectively, with a 20% decrease in intensity after only 10% water was added (Figs. 2d and e). As the water content reaches 80%, the fluorescence was almost illegible (Fig. 2f). The fluorescence profiles of R-CQD in different solvents were also recorded, and a significant decrease in fluorescence with increasing polarity was also observed (Fig. S3 in Supporting information). This suggests that R-CQD has a significant solvatochromic effect, *i.e.*, the fluorescence is red-shifted and quenched with increasing polarity, resulting in high possibility for cell imaging with high contrast and convenient wash-free imaging nature.

We then tested the stability of R-CQD, which showed a decrease in fluorescence of about only 5% after up to 40 min of light exposure, while the commercial probe BODIPY493/503 showed a 35% decrease (Fig. 2g). This suggests that R-CQD is high potential for long-term monitoring compared to existing commercial probes. In addition, R-CQD has bright fluorescence at pH 10, and the intensity is enhanced with increasing acidity (Fig. 2h). Moreover, common metal ions did not quench the fluorescence of R-CQD (Fig. 2i). Remarkably, the fluorescence intensity was enhanced by nearly 60% in the presence of Fe^{2+}. As one of native properties of phen is specifically chelating with Fe^{2+} to obtain red fluorescence, this phenomenon proves that phen is retained on the surface of R-CQD to contribute to the red-shifting fluorescence of R-CQD.

Drawing on the outstanding fluorescence properties of R-CQD, we assessed its cytotoxicity across various concentrations using HeLa and HepG2 cells (Fig. S4 in Supporting information). The results showed that even after 24 h of co-incubation with 40 μg/mL of R-CQD, the cells maintained nearly 90% high activity. We then further investigated its imaging ability in living cells by confocal laser scanning microscopy (CLSM). First, HeLa cells were stained with different concentrations (10–50 μg/mL) of R-CQD. As depicted in the CLSM images in Fig. S5 (Supporting information), R-CQD exceeding 10 μg/mL exhibited numerous bright spot-like fluorescent signals in the cytoplasm. Considering the negligible interference with cell activity at this concentration, subsequent cell imaging experiments were conducted using 10 μg/mL of R-CQD.

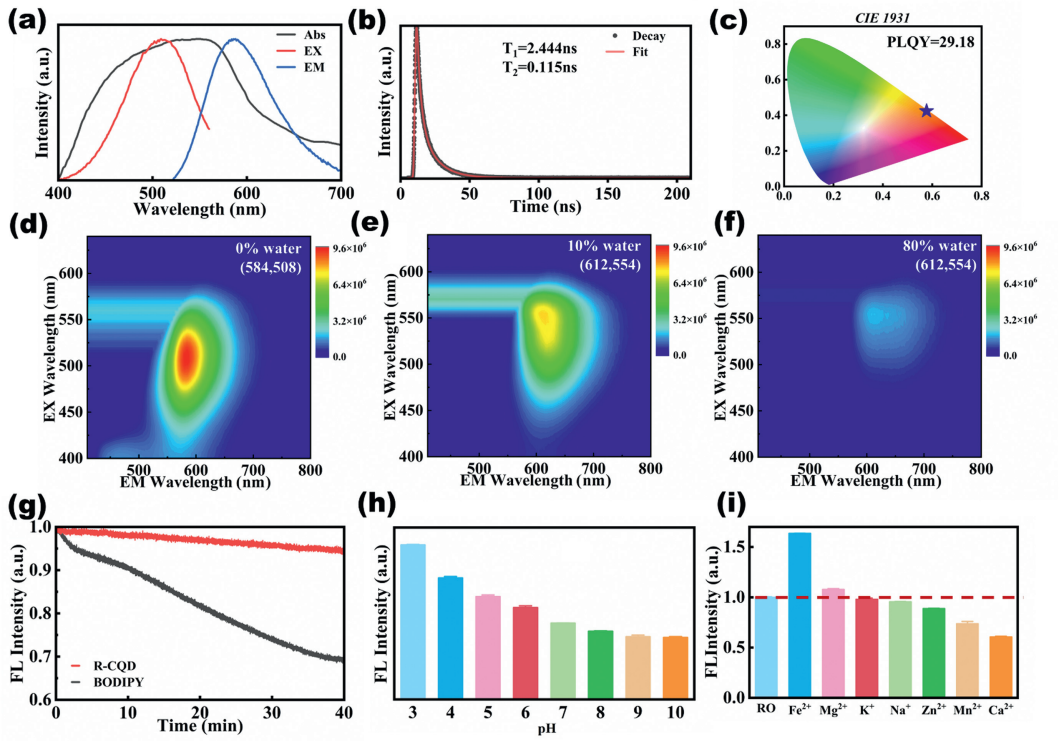

Fig. 2. Fluorescent properties of R-CQD. (a) absorption, excitation and emission spectra of R-CQD in glyceryl trioleate. (b) Fluorescence lifetime spectra in glyceryl trioleate. (c) CIE1931 coordinates in glyceryl trioleate. (d–f) The excitation-emission matrices of R-CQD in the mixture of H_2O and 1,4-dioxane. (g) Kinetics of R-CQDs and BODIPY. (h) Fluorescence intensity in different pH solutions. (i) Fluorescence intensity in a solution containing metal ion. Error bars represent the standard deviation (SD) for $n = 3$.

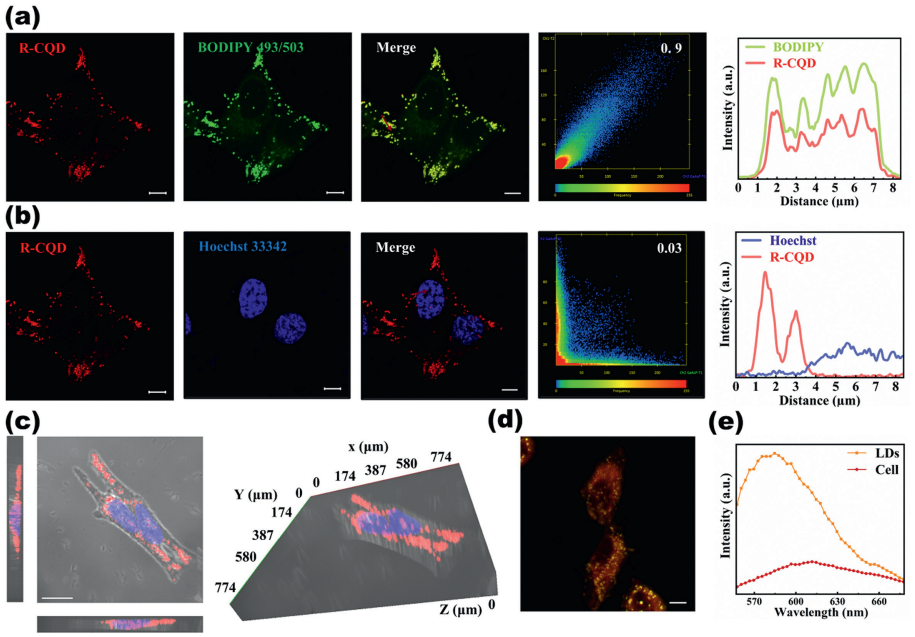

Fig. 3. LDs targeting property. Confocal fluorescence images and co-localization characterization Images of HeLa cells co-stained with R-CQD and commercial organelle probes (a) BODIPY 493/503 and (b) Hoechst 33342. (c) 3D images of HeLa cells co-stained with Hoechst 33342 and R-CQD (vertical, main, and left views). (d) True-color fluorescence images of live HeLa cells stained with R-CQD. (e) *In-situ* fluorescence spectra of the LD and cytoplasm in HeLa cells. Scale bar: 10 μm.

We then validated the LD-specific target monitoring ability of R-CQD through co-localization experiments on HeLa and HepG2 cells using the commercial LD probe BODIPY493/503 and the commercial cell probe Hoechst 33342 (Figs. 3a and b, Fig. S6a in Supporting information). It is worth noting that the high QY of the R-CD allows the monitoring process to be performed at more conservative parameter settings. The red fluorescence of R-CQD overlapped well with the green fluorescence of BODIPY493/503 in both HeLa and HepG2 cells, with a co-localization coefficient greater than 0.9, while there was almost no overlap with the blue fluorescence of Hoechst 33342 (co-localization coefficient of about 0.1), confirming the good LD-specificity of R-CQD. Three-dimensional (3D) images clearly showed the positional relationship between nuclei and LDs (Fig. 3c and Fig. S6b in Supporting information), indicating that

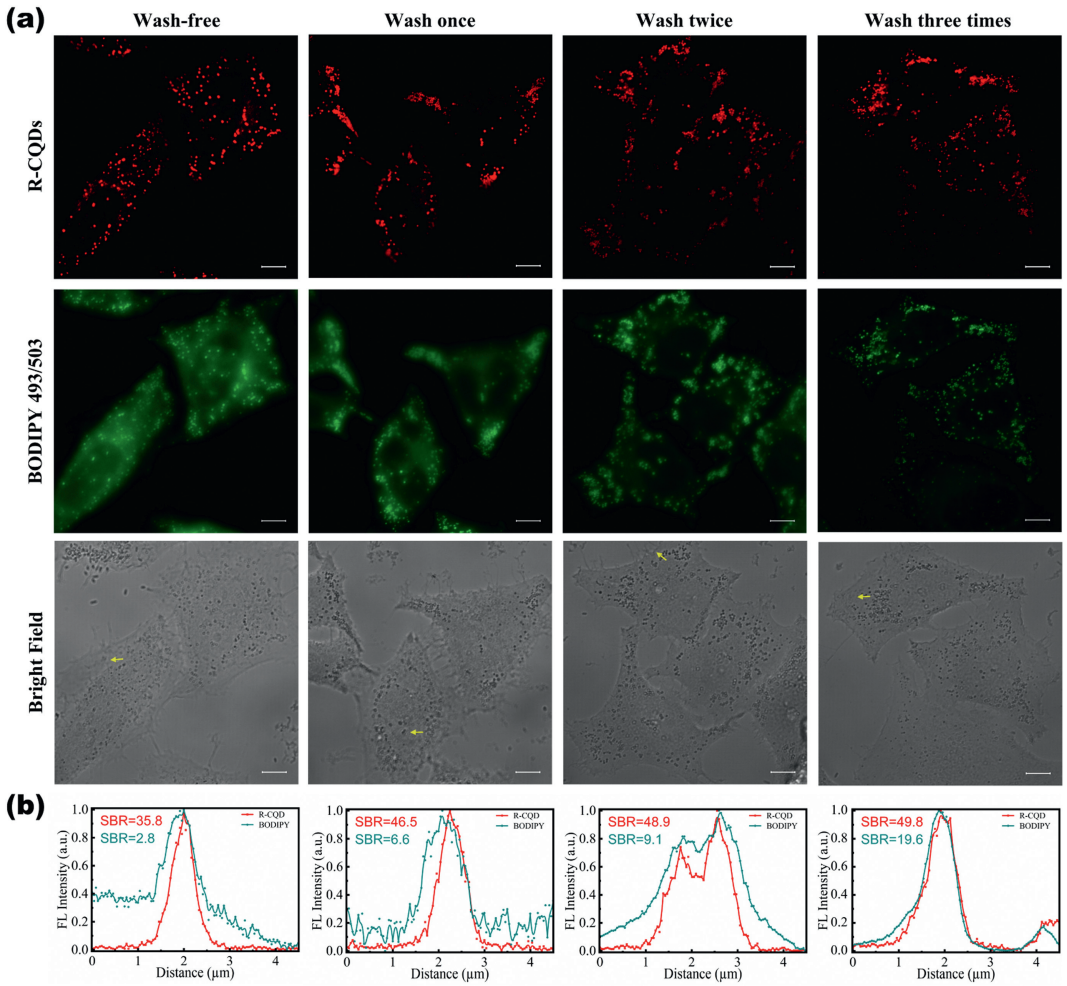

Fig. 4. Comparison of Wash-Free Imaging Capabilities. (a) CLSM images of HeLa cells stained with R-CQD and BODIPY 493/503 after washing without and with PBS. The yellow arrows indicate selected regions of fluorescence intensity profiles. (b) Signal-to-background ratio obtained by (a). Scale bar: 10 μm.

R-CQD can provide high-precision spatial localization information of LDs. Finally, we captured true-color fluorescence images of R-CQD-stained HeLa cells (Fig. 3d) and recorded the *in-situ* fluorescence spectra of the LDs and cytoplasm (Fig. 3e). The results showed that R-CQD emitted bright 590 nm fluorescence at the LDs, whereas there was a weak background signal at 610 nm in the cells, demonstrating that R-CQD can accurately target LDs and provide clear and precise fluorescence information.

To further prove the long-term dynamic monitoring ability, we also measured the change in fluorescence brightness within 40 min after R-CQD staining of HeLa cells (Fig. S7 in Supporting information). The results demonstrated that the cells exhibited bright fluorescence within the LDs immediately after the addition of R-CQD, and this brightness remained stable for the entire 40-min period. This indicates that the suitable amphiphilicity of R-CQD enables rapid diffusion in various environments and retention within the LDs.

Due to the excellent solvatochromic effect of R-CQD, which exhibits only weak fluorescence in the aqueous environment, it could achieve convenient wash-free imaging, enabling a more efficient imaging process than that of commercial probes such as BODIPY 493/503. To this merit, we co-labeled HeLa cells with R-CQD and BODIPY 493/503, then captured fluorescence images of the two channels wash-free and after different times of phosphate buffered saline (PBS) washes, respectively [50]. The results in Fig. 4a show that R-CQD does not produce much background interference even without PBS washing, while BODIPY 493/503 requires three times PBS washes for similar results. Further statistics revealed that even without washing, R-CQD provided a signal-to-background ratio (SBR) of more than 30, surpassing that of the BODIPY 493/503 channel after three times washes (Fig. 4b). This result demonstrates that R-CQD is an excellent and versatile probe for ultrafast and wash-free fluorescence imaging of LDs.

In the context of long-term monitoring of living cells, the preference often leans towards dyes with extended excitation wavelengths to mitigate the risk of photodamage during imaging. The above characterization of R-CQD in LDs has shown that it can be excited by 543 nm laser light, representing an 11.3% redshift compared to the 488 nm commonly used in BODIPY 493/503. It has been shown that the gap in cellular damage caused by a small change in the wavelength of the irradiated laser can be dramatic, *e.g.*, even a brief irradiation with a low-power 405 laser may lead to irreversible cell death [26]. Considering that R-CQD itself has significantly stronger resistance to photobleaching than BODIPY 493/503, we again tested the safety of R-CQD for long-term monitoring of cells. As shown in Fig. S8a (Supporting information), the HeLa cells were co-labeled with R-CQD and BODIPY 493/503 and continuously imaged. The 543 nm laser irradiation showed no significant change in the cell morphology after 30 min, and the cell morphology remained stable even within 1 h (Fig. S8b in Supporting information), while in contrast, the cells appeared to have a large number of blebs after 10 min irradiation by the 488 laser

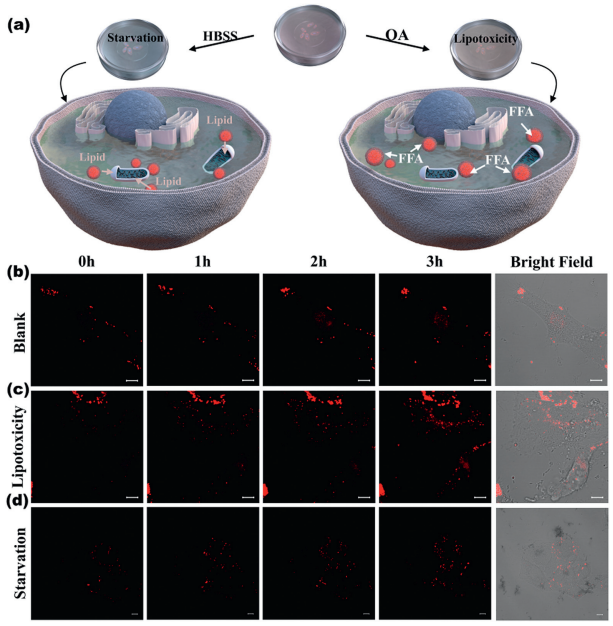

Fig. 5. Long-term monitoring of HeLa cell under diverse pathological conditions. (a) Schematic representation of changes in LDs of HeLa cells in different pathological states. (b) CLSM images of HeLa cells in normal state over a period of 3 h. (c) CLSM images of HeLa cells in 3 h after addition of 0.5 mmol/L OA. (d) CLSM images of HeLa cells in 3 h after starvation treatment. Scale bar: 10 μm.

(Fig. S8c in Supporting information), which is usually regarded as a distinctive feature of apoptosis [51,52], and the blebs increased significantly. Therefore, R-CQD demonstrates the superior capability for long-term tracking of LDs with a 543 nm laser, a challenging task for BODIPY 493/503 (Fig. S8d in Supporting information).

Encouraged by the excellent fluorescence imaging performance, R-CQD was further utilized to monitor the dynamics of LDs in different biological processes (Fig. 5a). Initially, we recorded CLSM images of R-CQD-labeled HeLa cells within 3 h as a blank group. As shown in Fig. 5b, the morphology of the cells did not change significantly within 3 h, and the morphology and distribution of LDs remained stable. The R-CQD always localized in the LDs during the whole process, and the fluorescence did not show significant quenching, indicating that the R-CQD is suitable for long-term tracking of LDs. It is well known that excessive free fatty acids (FFAs) enriched in organelles such as mitochondria or endoplasmic reticulum may affect the normal physiological activities, triggering oxidative stress and even cell death. Therefore, when FFA increases in the environment, LD would initiate active enrichment of FFA to avoid lipotoxicity [53]. So 0.5 mmol/L oleic acid (OA) was added to R-CQD-labeled HeLa cells to stimulate the production of more LDs by FFA. As shown in Fig. 5c, a significant increase in the number of LDs in the cells was successfully recorded within 3 h. The nascent LDs were uniformly distributed inside the cells, and their volume also gradually increased (Fig. S9a in Supporting information). The increase and enlargement of LDs during OA treatment further inspired us to explore the LDs changes in a new biological process of starvation. Next HeLa cells were labeled with R-CQD and then the medium was replaced with Hanks' balanced salt solution (HBSS) to induce starvation culture. As shown in Fig. 5d, it can be clearly observed that the number of intracellular LDs increased with prolonged starvation treatment (Fig. S9a in Supporting information), unlike the OA-treated group, the intracellular LDs in the starved group were not dispersed homogeneously throughout the cells but tended to be enriched in certain locations with a much smaller average size (Fig. S9b in Supporting information). This may be due to the fact that cells under starvation need to catabolize lipids for energy in a nutrient-poor environment, and thus FFA in the cytoplasm was enriched into dense and small-volume LDs for lysosomes and mitochondria, which is in line with the process previously reported in the literature [54,55]. The above results suggest that the morphological changes and dynamic information of LDs observed with the help of R-CQD may contribute to further understanding of the physiological functions of LDs.

In summary, we have developed R-CQD, an efficient LD-specific probe with excellent optical properties using a solvothermal strategy. Importantly, red fluorescence significantly reduces phototoxic damage to cells from long-term monitoring. Benefiting from the excellent biocompatibility, outstanding fluorescence properties, high photostability, and remarkable solvatochromism, R-CQDs were successfully applied for wash-free targeted imaging LDs in living cells for long-term monitoring. This stability and safety monitoring capability enable successful and dynamic visualization of LDs during oleic acid induced lipotoxicity and starvation treatment in a long term of 3 h. We believe that the findings presented in this work hold great significance for understanding the mechanism of LD regulation in living cells, providing an effective tool for studying related diseases.

Declaration of competing interest

The authors declare that they have no known competing financial interests or personal relationships that could have appeared to influence the work reported in this paper.

Acknowledgments

This work was supported by the National Natural Science Foundation of China (Nos. 52003178, 52273141 and 51973132) and Natural Science Foundation of Sichuan Province (No. 2023NSFSC0338).

Supplementary Materials

Supplementary material associated with this article can be found, in the online version, at 10.1016/j.cclet.2024.109523.

References

[1] S. Wang, W.X. Ren, J.T. Hou, et al., Chem. Soc. Rev. 50 (2021) 8887–8902.
[2] E.A. Specht, E. Braselmann, A.E. Palmer, Annu. Rev. Physiol. 79 (2017) 93–117.
[3] Z. Cai, L. Zhu, M. Wang, et al., Theranostics 10 (2020) 4265–4276.
[4] J. Huang, C. Xie, X. Zhang, et al., Angew. Chem. Int. Ed. 58 (2019) 15120–15127.
[5] S. Chang, L.Y. Liang, Y.T. Gao, et al., Trends Analyt. Chem. 168 (2023) 117325.
[6] M. Tian, Y. Ma, W. Lin, et al., Acc. Chem. Res. 52 (2019) 2147–2157.
[7] X.Y. Sun, T. Liu, J. Sun, X.J. Wang, RSC Adv. 10 (2020) 10826–10847.
[8] J.F. Dekkers, M. Alieva, L.M. Wellens, Nat. Protoc. 14 (2019) 1756–1771.
[9] J.C. Thiele, D.A. Helmerich, N. Oleksiievets, et al., ACS Nano 14 (2020) 14190–14200.
[10] Y. Chen, P. Pei, Z. Lei, et al., Angew. Chem. Int. Ed. 133 (2021) 15943–15949.
[11] M. Chen, Z. Feng, X. Fan, et al., Nat. Commun. 13 (2022) 6643.
[12] S. Liu, L.M. Tay, R. Anggara, Y.J. Chuah, Y. Kang, ACS Appl. Mater. Interfaces 8 (2016) 11925–11933.
[13] S. Samanta, K. Lai, F. Wu, et al., Chem. Soc. Rev. 52 (2023) 7197–7261.
[14] B. Unnikrishnan, R.S. Wu, S.C. Wei, C.C. Huang, H.T. Chang, ACS Omega 5 (2020) 11248–11261.
[15] H. Ali, S. Ghosh, N.R. Jana, Wiley Interdiscip. Rev. Nanomed. Nanobiotechnol. 12 (2020) e1617.
[16] X. Li, S. Zhao, B. Li, et al., Coord. Chem. Rev. 431 (2021) 213686.
[17] X. Yang, X. Li, B. Wang, et al., Chin. Chem. Lett. 33 (2022) 613–625.
[18] S. Mei, X. Wei, Z. Hu, et al., Opt. Mater. 89 (2019) 224–230.
[19] B. Wang, G.I.N. Waterhouse, S. Lu, Trends Chem. 5 (2023) 76–87.
[20] M. Fang, B. Wang, X. Qu, et al., Chin. Chem. Lett. 35 (2024) 108423.
[21] N. Xin, D. Gao, B. Su, et al., ACS Sens. 8 (2023) 1161–1172.
[22] L. Wu, X. Li, Y. Ling, C. Huang, N. Jia, ACS Appl. Mater. Interfaces 9 (2017) 28222–28232.
[23] S. E, X. Q, X.L. Mao, Yuan, et al., Nanoscale 10 (2018) 12788–12796.
[24] G. Zou, S. Chen, N. Liu, Y. Yu, Chin. Chem. Lett. 33 (2022) 778–782.
[25] D. Gao, Y. Zhang, K. Wu, et al., Biosens. Bioelectron. 200 (2022) 113928.
[26] J. Icha, M. Weber, J.C. Waters, C. Norden, Bioessays 39 (2017) 1700003.
[27] P.P. Laissue, R.A. Alghamdi, P. Tomancak, E.G. Reynaud, H. Shroff, Nat. Methods 14 (2017) 657–661.

[28] R.A. Hoebe, C.H. Van Oven, T.W. Gadella, et al., Nat. Biotechnol. 25 (2007) 249–253.
[29] X. Wei, D. Yang, L. Wang, et al., Colloids Surf. B 220 (2022) 112869.
[30] S. Douthwright, G. Sluder, J. Cell. Physiol. 232 (2017) 2461–2468.
[31] J.A. Olzmann, P. Carvalho, Nat. Rev. Mol. Cell Biol. 20 (2018) 137–155.
[32] F. Wilfling, J.T. Haas, T.C. Walther, R.V. Farese Jr, Curr. Opin. Cell Biol. 29 (2014) 39–45.
[33] H.F. Hashemi, J.M. Goodman, Curr. Opin. Cell Biol. 33 (2015) 119–124.
[34] Y.G. Jeon, Y.Y. Kim, G. Lee, J.B. Kim, Nat. Metab. 5 (2023) 735–759.
[35] Y. Guo, K.R. Cordes, R.V. Farese Jr, T.C. Walther, Cell Physiol. 122 (2009) 749–752.
[36] N. Hammoudeh, C. Soukkarieh, D.J. Murphy, A. Hanano, Prog. Lipid Res. 91 (2023) 101233.
[37] J. Marschallinger, T. Iram, M. Zardeneta, et al., Nat. Neurosci. 23 (2020) 194–208.
[38] M. Ramosaj, S. Madsen, V. Maillard, et al., Nat. Commun. 12 (2021) 7362.
[39] P.T. Bozza, J.P. Viola, Prostaglandins Leukot. Essent. Fatty Acids 82 (2010) 243–250.
[40] Q. Liu, Q. Luo, A. Halim, G. Song, Cancer Lett. 401 (2017) 39–45.
[41] Y. Minami, A. Hoshino, Y. Higuchi, et al., Nat. Commun. 14 (2023) 4084.
[42] S. Beloribi-Djefaflia, S. Vasseur, Oncogenesis 5 (2016) e189.
[43] Z. Zheng, Y. Yang, P. Wang, et al., Adv. Funct. Mater. 33 (2023) 2303627.
[44] L. Yang, J. Wang, B. Liu, et al., Sens. Actuator. B: Chem. 333 (2021) 129541.
[45] X. Wei, S. Mei, D. Yang, et al., Nanoscale Res. Lett. 14 (2019) 172.
[46] L. Tang, L. Ai, Z. Song, et al., Adv. Funct. Mater. 33 (2023) 2303363.
[47] J. Ge, Q. Jia, W. Liu, et al., Adv. Mater. 27 (2015) 4169–4177.
[48] H. Sun, P. Xia, H. Shao, et al., J. Colloid Interface Sci. 646 (2023) 932–939.
[49] H. Cai, X. Wu, L. Jiang, et al., Chin. Chem. Lett. 35 (2024) 108946.
[50] J. Wang, Y. Guo, X. Geng, et al., ACS Appl. Mater. Interfaces 13 (2021) 44086–44095.
[51] M.L. Coleman, E.A. Sahai, M. Yeo, et al., Nat. Cell Biol. 3 (2001) 339–345.
[52] V. Magidson, A. Khodjakov, Methods Cell Biol. 114 (2013) 545–560.
[53] T.B. Nguyen, J.A. Olzmann, Autophagy 13 (2017) 2002–2003.
[54] T.B. Nguyen, S.M. Louie, J.R. Daniele, et al., Dev. Cell 42 (2017) 9–21 1.
[55] I.Y. Benador, M. Veliova, M. Liesa, O.S. Shirihai, Cell Metab. 29 (2019) 827–835.